International Journal of Minerals, Metallurgy and Materials
Volume 26, Number 2, February 2019, Page 202
https://doi.org/10.1007/s12613-019-1725-9

Mechanical and corrosion properties of low-carbon steel prepared by friction stir processing

Li-ying Huang[1,2)], *Kuai-she Wang*[1,2)], *Wen Wang*[1,2)], *Kai Zhao*[1,2)], *Jie Yuan*[1,2)], *Ke Qiao*[1,2)], *Bing Zhang*[1,2)], *and Jun Cai*[1,2)]

1) School of Metallurgical Engineering, Xi'an University of Architecture and Technology, Xi'an 710055, China

2) National and Local Joint Engineering Research Center for Functional Materials Processing, Xi'an University of Architecture and Technology, Xi'an 710055, China

(Received: 9 April 2018; revised: 6 June 2018; accepted: 11 June 2018)

Abstract: Low-carbon steel plates were successfully subjected to normal friction stir processing (NFSP) in air and submerged friction stir processing (SFSP) under water, and the microstructure, mechanical properties, and corrosion behavior of the NFSP and SFSP samples were investigated. Phase transformation and dynamic recrystallization resulted in fine-grained ferrite and martensite in the processed zone. The SFSP samples had smaller ferrites (5.1 μm), finer martensite laths (557 nm), and more uniform distribution of martensite compared to the NFSP samples. Compared to the base material (BM), the microhardness of the NFSP and SFSP samples increased by 19.8% and 27.1%, respectively because of the combined strengthening effects of grain refinement, phase transformation, and dislocation. The ultimate tensile strengths (UTSs) of the NFSP and SFSP samples increased by 27.1% and 38.7%, respectively. Grain refinement and martensite transformation also improved the electrochemical corrosion properties of the low-carbon steel. Overall, the SFSP samples had better mechanical properties and electrochemical corrosion resistance than the NFSP samples.

Keywords: low-carbon steel; friction stir processing; microstructure; mechanical properties; corrosion

1. Introduction

Low-carbon steels are widely used in automobiles, constructions, and other industrial fields [1] because of their abundance, low cost, ease of smelting, and good formability [2–3]. However, their industrial application is limited by low hardness, strength, and corrosion resistance [4].

Friction stir processing (FSP) is a new severe plastic deformation (SPD) technique [5] developed based on friction stir welding (FSW) [6–8], during which the material is broken and mixed under the intense plastic deformation. At such conditions the grains become refined because of dynamic recrystallization [9]. Under forced cooling conditions, ultra-fine and even nano-sized grains can be obtained [10–12]. Additionally, FSP is a simple and environment-friendly technology and can be used to prepare large-area ultrafine-grained plates [13].

In the past, most of the FSP/FSW-related research focused mainly on magnesium [14] and aluminum [8] alloys as well as other low-melting metals. Although several studies have investigated FSP/FSW for various steels (e.g., interstitial free steel [15], stainless steel [16], super-austenitic steel [17], and structural steel [18]), there are only few studies on FSP of low-carbon steels. Sekban *et al.* [19] found that the ferrite grain size of a low-carbon steel decreased from 25 to 3 μm during FSP. The grain refinement increased the strength, which was tested under uniaxial loading. In addition to the grain refinement, the phase transformation during FSP also affects the mechanical properties of low-carbon steels. In another study, the same group of authors also demonstrated that the structures of the stir zone and heat-affected zone mainly comprised martensite, ferrite, Widmanstätten ferrite, and a mixture of ferrite and cementite, while the structure of base material (BM) consisted only of ferrite and pearlite; the microstructural changes improved the hardness and strength [20].

Grain refinement and phase transformation also affect corrosion properties [21]. Zhang *et al.* [22], as well as few other researchers, have studied FSW effects on friction-stir

Corresponding authors: Kuai-she Wang E-mail: wangkuaishe888@126.com; Wen Wang E-mail: wangwen2016@126.com

welded joints of high nitrogen-content stainless steel, considering microstructural evolution and pitting corrosion behavior; they observed that FSW could reduce the coarse inclusions and refine the grains, thus improving the pitting resistance of friction-stir welded joints. However, to the best of our knowledge, there is no related research on the corrosion property of low-carbon steels prepared by FSP, which is mostly because of the difficulty of processing and complex phase transformation during FSP.

Considering the engineering applications of low-carbon steels, their corrosion properties, in addition to the mechanical properties, should be improved. Thus, the goal of our study is to investigate the influences of normal friction stir processing (NFSP) in air and submerged friction stir processing (SFSP) under water on the microstructure, mechanical properties, and corrosion properties of low-carbon steels.

2. Experimental

2.1. Material and processing

For the experiments, 3 mm plate of Q235 low-carbon steel with a nominal chemical composition (wt%) of 0.18 C, 0.45 Mn, 0.03 Si, 0.045 P, and 0.055 S (balance: Fe) was used.

The low-carbon steel plates were subjected to NFSP and SFSP along the rolling direction of the plates. Both processes had the same parameters: rotation rate of 950 r/min, travel speed of 60 mm/min, and 0.2 mm thickness reduction. A WC cylindrical stir tool (without stir pin) with a flat shoulder of 14 mm diameter was used.

The microstructure of the processed zone (PZ) was examined by scanning electron microscopy (SEM, JSM-6700F) and transmission electron microscopy (TEM, JEM-200CX). The grain size of ferrite and width of the martensite laths were measured by linear intercept method. Samples for SEM were cut perpendicularly to the processing direction and then etched with a solution of 4vol% nitric acid + 96vol% alcohol. The samples for TEM were cut parallel to the processing direction, and the thin foils for TEM observations were prepared by double-jet electrolytic polishing in an electrolyte consisting of 100 mL perchloric acid and 900 mL alcohol. A 401 MVD sclerometer was used to measure the microhardness of the samples along the middle of the cross section under a load of 1.96 N for a dwell time of 10 s.

2.2. Room temperature tensile test

The room temperature tensile tests were conducted on an Instron 8801 testing machine at an initial strain rate of 1×10^{-3} s^{-1}. The samples were cut along the transverse direction, ensuring that the gauge section was located in the PZ (Fig. 1). Each set of tensile tests was conducted three times.

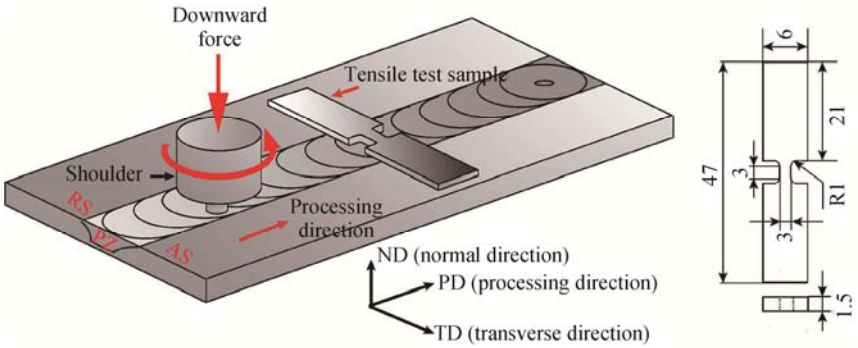

Fig. 1. Schematic of the FSP and dimension of the tensile test sample (mm). AS and RS represent advancing and retreating sides, respectively.

2.3. Electrochemical test

Potentiodynamic polarization curves and electrochemical impedance spectroscopy (EIS) were performed in 3.5wt% NaCl solution at room temperature using a PARSTAT4000 electrochemical analyzer. Samples with a dimension of 10 mm × 10 mm × 3 mm were cut from PZ. A three-electrode system, consisting of a platinum counter electrode, a saturated calomel electrode, and a working electrode, was used. Potentiodynamic polarization curve tests were performed in a scanning range of −0.5 to 1 V at a scanning rate of 1 $mV \cdot s^{-1}$. EIS tests were carried out at the open circuit potential using a sinusoidal wave with an amplitude of 10 mV at frequency range of 100 kHz to 10 mHz. The electrochemical corrosion morphology after cleaning (with a solution of HCl (50 mL) + distilled water (500 mL) + $C_6H_{12}N_4$ (3.5 g)) was observed by SEM. Each set of electrochemical corrosion tests was conducted three times.

The corrosion rate of each sample was calculated as the following [23]:

$$v = 3.27 \times 10^{-3} \times \frac{Mi_{corr}}{n\rho} \quad (1)$$

where v is the corrosion rate, mm/a; i_{corr} is the corrosion current density, $\mu A/cm^2$; ρ is the density of the working electrode, g/cm^3, M is the relative atomic mass, and n is the

charge number of the working electrode.

3. Results and discussion

3.1. Macrostructure

During FSP, plastic flow of the metal occurred under compressive and shear stresses applied by the shoulder of the stir tool. The plastic flow of the metal near the shoulder was larger because of the larger stress and frictional heat. The plastic flow became smaller farther away from the shoulder.

The cross sections of the NFSP and SFSP samples had a basin-like shape (Fig. 2), and three obvious regions could be distinguished: PZ, thermo-mechanically affected zone, and BM. Because of the cooling effect of water, frictional heat in the PZ dissipated more easily; therefore, the PZ area of the SFSP sample was smaller than that of the NFSP sample (Figs. 2(a) and 2(b)). The PZ depths of the NFSP and SFSP samples were 1.9 and 1.3 mm, respectively. The widths of the PZ on the top surface of both the NFSP and SFSP samples were 14 mm and were influenced by the shoulder. With an increase of the depth along the normal direction, the influence of the shoulder on the width of the samples decreased gradually, as well as the PZ width.

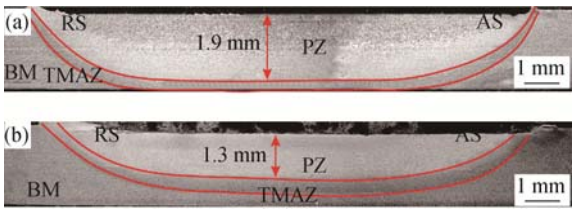

Fig. 2. Cross-sectional macrostructure of the NFSP (a) and SFSP (b) samples.

3.2. Microstructure

The microstructure of BM, NFSP, and SFSP samples (Fig. 3) show that the BM sample mainly comprised ferrite and pearlite. The equiaxed ferrite grains were coarse and non-uniformly distributed, and the average grain size of the

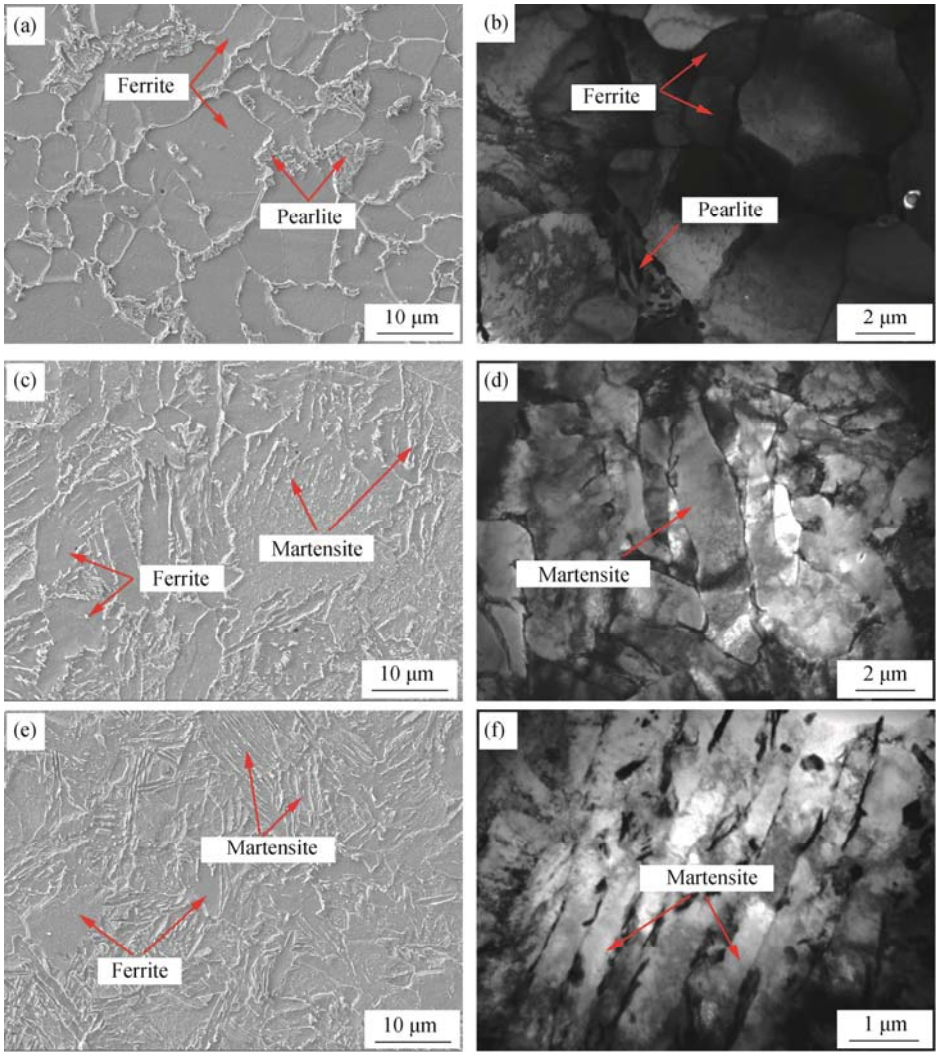

Fig. 3. SEM (a, c, e) and TEM (b, d, f) images of the samples: (a, b) BM; (c, d) NFSP; (e, f) SFSP.

ferrite was about 11.3 μm (Fig. 3(a)). Pearlites were mainly distributed along the ferrite grain boundaries (Fig. 3(b)). However, the microstructure of the NFSP sample changed significantly compared to that of the BM sample, and a dual-phase microstructure comprising ferrite and martensite was observed (Fig. 3(c)). The average width of the martensite laths was 1.5 μm (Fig. 3(d)). The phase transformation during NFSP of the low-carbon steel indicates that the processing temperature is higher than A_{c1} (The temperature at which the ferrite begins to transform into austenite during heating) [24–25]. At this temperature range, some of the initial ferrite transformed into austenite and then into martensite during the subsequent cooling. Dynamic recrystallization of ferrite occurred during NFSP, and its final average grain size was 7.8 μm.

The microstructure of the SFSP sample is similar to that of the NFSP sample: both had a dual-phase microstructure consisting of ferrite and martensite (Fig. 3(e)). However, because of the faster cooling rate, the ferrite grains of the SFSP sample were finer with an average grain size of 5.1 μm. Additionally, the SFSP sample had more lath martensite with uniform distribution, and its laths were finer with an average width of 557 nm (Fig. 3(f)).

3.3. Microhardness and tensile properties

Fig. 4 shows the microhardness of the cross sections of the BM, SFSP, and NFSP samples. The average microhardness values in the PZ of the NFSP and SFSP samples were HV 160.1 and HV 169.8, respectively, which are 19.8% and 27.1% higher than that of the BM sample, respectively. These differences are attributed to the ferrite grain refinement and martensite transformation. The SFSP sample had a higher microhardness than the NFSP sample because of further refinement of ferrite grains, increase of martensite content, and finer martensite laths.

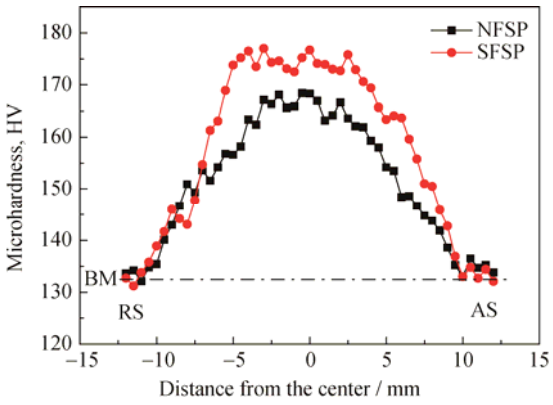

Fig. 4. Distribution of microhardness in cross-section of the BM, NFSP, and SFSP samples.

Fig. 5 shows stress–strain curves of the BM, NFSP, and SFSP samples at room temperature, and the tensile strength test results are summarized in Table 1. The ultimate tensile strengths (UTS) of the low-carbon steel increased significantly after NFSP and SFSP, while the elongation to failure (EL) decreased only slightly. The UTS and EL of the BM sample was 470 MPa and 51.4%, respectively. Compared with BM, the UTS of the NFSP and SFSP samples increased by 27.0% and 38.7%, respectively. The ELs of the NFSP and SFSP sample were 47.1% and 45.6%, respectively, which is slightly lower than that of the BM.

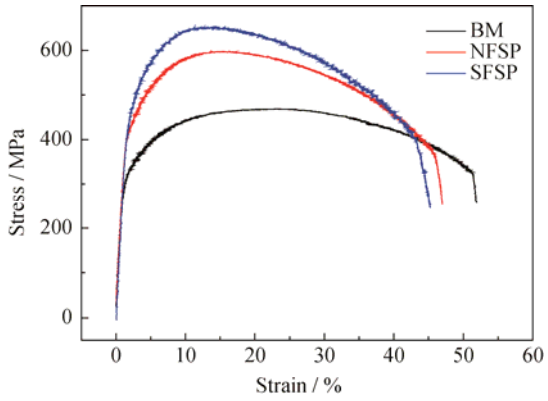

Fig. 5. Stress–strain curves of the BM, NFSP, and SFSP samples.

Table 1. Tensile strength test results for low-carbon steel at room temperature

Sample	UTS / MPa	EL / %
BM	470 ± 2	54.1 ± 0.2
NFSP	597 ± 4	47.1 ± 0.3
SFSP	652 ± 2	45.6 ± 0.2

The ferrite grains of both NFSP and SFSP samples seemed noticeably refined. At the same time, lath martensite appeared in the samples. Martensite has a high hardness and strength; therefore, the strengthening of grain refinement, dislocation, and the presence of a secondary phase made the UTSs of the two samples much higher than that of the BM sample. The UTS of the SFSP sample is higher than that of the NFSP sample because of the higher content of finer lath martensite and its more uniform distribution. Moreover, the fine grains can prevent crack propagation [26]; therefore, the plasticity of the FSP-treated low-carbon steel is improved. On the other hand, the lath martensite formed in low-carbon steels has a low carbon content and uniform carbide distribution, as well as an uneven dislocation distribution and a low-density dislocation zone, which provides space for dislocation activity. The dislocation motion can alleviate the

local stress concentration. Therefore, the strength of low-carbon steels increases after FSP, yet the plasticity does not decrease noticeably [27].

Strength and elongation are important mechanical properties of low-carbon steels, and they are often inversely proportional: the elongation decreases with an increase of strength. In low-carbon steels prepared by other SPD techniques, elongation also decreases significantly with an increase in strength. Lee *et al.* [28] reported that the UTS of a low-carbon steel prepared by accumulative roll-bonding technology was about three times higher than that of the BM, and the elongation dropped largely from 60% to <20%. Singh *et al.* [29] prepared a high-strength ultrafine-grained low-carbon steel by equal channel angular pressing and found that the UTS increased from 367 to 1009 MPa, while the elongation decreased from 41% to 1%. They demonstrated that the main reason for the low ductility of the SPD-fabricated fine-grained materials was the high dislocation density. However, the fine-grained materials prepared by FSP had a much lower ductility loss, which was mainly because of a low dislocation as well as a high ratio of high-angle grain boundaries.

3.4. Electrochemical corrosion

3.4.1. Potentiodynamic polarization curve and EIS tests

Fig. 6(a) shows potentiodynamic polarization curves of the BM, NFSP, and SFSP samples. Corrosion potentials (E_{corr}), corrosion current densities (i_{corr}), and corrosion rates (v, calculated by Eq. (1)) are summarized in Table 2. Values of E_{corr}, i_{corr}, and v of the NFSP and SFSP samples are both lower than those of the BM sample, and values of E_{corr}, i_{corr}, and v of the SFSP sample are lower than those of the NFSP sample. The decrease of corrosion potential indicates that FSP-prepared low-carbon steel is more susceptible to corrosion and can more easily form a passive film. The density of the passive film directly affects the corrosion rate.

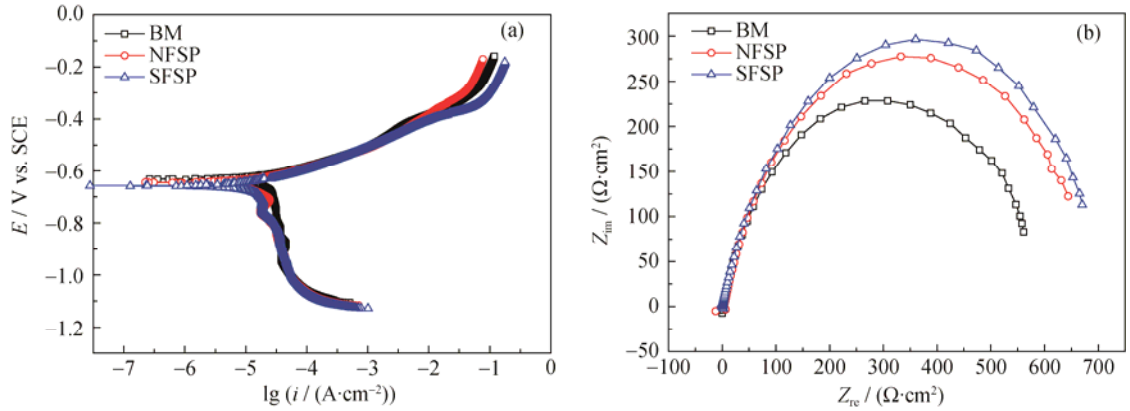

Fig. 6. Potentiodynamic polarization curves (a) and Nyquist plots (b) of the BM, NFSP, and SFSP samples in 3.5wt% NaCl solution.

Table 2. Electrochemical parameters for the BM, NFSP, and SFSP samples

Sample	E_{corr} / mV	i_{corr} / (μA·cm^{-2})	v / (mm·a^{-1})
BM	–632.6	31.5	0.367
NFSP	–644.3	16.2	0.189
SFSP	–656.9	14.3	0.167

Meanwhile, the Nyquist plots (Fig. 6(b)) of the NFSP, SFSP, and BM samples only show capacitive loops, whereby the same electrochemical corrosion behavior is demonstrated for all three samples. Generally, the larger the diameter of a capacitive loop, the higher the corrosion resistance. Based on the experimental results of polarization and EIS tests, it can be concluded that the corrosion resistances of the NFSP and SFSP samples are both higher than that of the BM sample. The SFSP sample has the best corrosion resistance.

Nyquist plots of the NFSP and SFSP samples were fitted by Zsimpwin software to obtain an equivalent electrical circuit (EEC), which is shown in Fig. 7. Both samples have the same EEC, indicating the same corrosion mechanism. In the EEC diagram, R_s is the solution resistance, R_t is the charge transfer resistance, Q is the constant phase angle element, and n is the dispersion coefficient. R_t is an important index for corrosion resistance evaluation. The higher the R_t value, the denser the passive film and the stronger the resistance to ion and charge conduction. R_t has an inverse relationship with the corrosion rate.

Table 3 summarizes the fitting values of the EEC components. The R_t values decrease in the following order: SFSP > NFSP > BM. Thus, the SFSP sample is more resistant to corrosion, followed by the NFSP and then BM

samples. These results agree with the potentiodynamic polarization curve and EIS results.

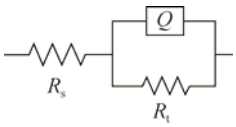

Fig. 7. Equivalent electrical circuit of the EIS.

Table 3. Fitting values of the equivalent electrical circuit components

Samples	R_s / ($\Omega \cdot cm^2$)	Q / (10^{-4} F·cm^{-2})	n	R_t / ($\Omega \cdot cm^2$)
BM	3.417	4.726	0.8475	581.7
NFSP	6.487	3.712	0.8534	685.9
SFSP	0.625	7.164	0.8482	711.7

3.4.2. Electrochemical corrosion morphology

Fig. 8 shows SEM images of the electrochemical corrosion morphologies of the BM, NFSP, and SFSP samples. The most severe corrosion was in the BM sample, as its corrosion pits were more abundant, bigger, and deeper (Fig. 8(a)). This severe pitting corrosion was very uniform (Fig. 8(b)).

Corrosion morphology changed noticeably after FSP. Less corrosion pits were observed in the NFSP sample, which were smaller and much shallower (Fig. 8(c)). The corrosion degree and surface roughness of the whole sample was not as severe as that of the BM sample (Fig. 8(d)); thus, the electrochemical corrosion resistance of the NFSP sample was improved.

The change of the electrochemical corrosion morphology of the SFSP sample was especially noticeable (Figs. 8(e) and 8(f)). The number of pits on the surface of SFSP sample was further reduced, and the pits were the smallest and shallowest. These characteristics are consistent with the results of potentiodynamic polarization curve and EIS tests, which indicate that FSP can improve electrochemical corrosion resistance of low-carbon steels, especially SFSP.

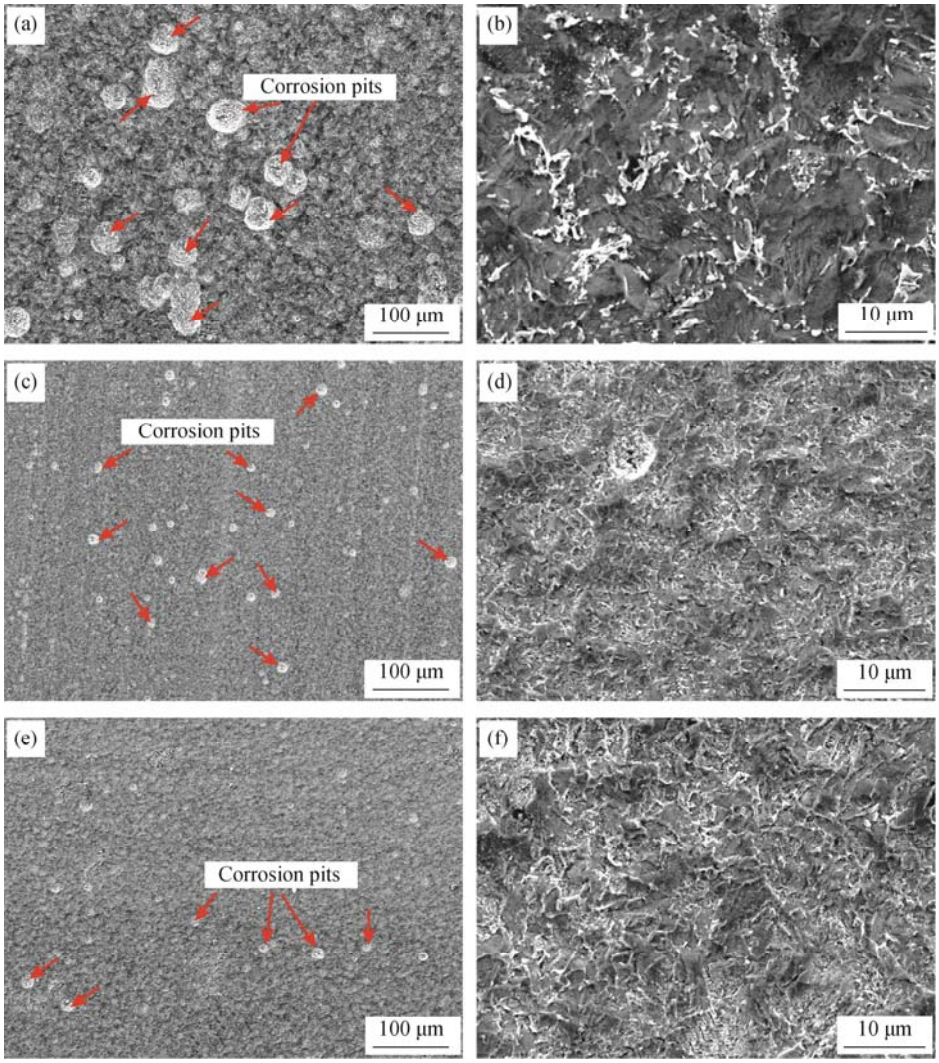

Fig. 8. Electrochemical corrosion morphologies of the samples: (a, b) BM; (c, d) NFSP; (e, f) SFSP.

Grain refinement and martensite formation after FSP are beneficial for the formation of dense passive films [30]; therefore, the corrosion resistance of FSP-treated low-carbon steels is improved. The effects of grain size and martensite on the corrosion properties of steels have been studied extensively by other researchers, and the same conclusion was obtained. Ura-Bińczyk *et al.* [31] reported N80-1 steel to be more corrosion-resistant than K55 steel because grain refinement results in a denser and more uniform passive film on the N80-1 steel surface. Bai *et al.* [32] reported that the heat-affected zone of high-strength low-alloy steel welded by underwater wet welding had a coarse tempered martensite structure, which was beneficial for a dense passive film formation and for corrosion resistance improvement.

4. Conclusions

A low-carbon steel was successfully subjected to NFSP and SFSP, and the microstructure, mechanical, and electrochemical corrosion properties of the steel were studied. The main conclusions are as follows.

(1) The microstructures of the samples after NFSP and SFSP changed; they showed a dual-phase fine-grained material consisting of ferrite and lath martensite. The SFSP sample had finer ferrite grains and martensite laths compared to the NFSP sample.

(2) The strengthening of the grain refinement, dislocation, secondary phase improved the mechanical properties of the NFSP and SFSP samples. Compared to the BM sample, the microhardness of the NFSP and SFSP samples increased by 19.8% and 27.1%, respectively, and the UTSs of the NFSP and SFSP samples increased by 27.1% and 38.7%, respectively.

(3) The refinement of ferrite grains and formation of martensite during NFSP and SFSP resulted in the formation of denser passive films, which improve corrosion resistance. Compared to the NFSP sample, the SFSP sample showed better electrochemical corrosion resistance.

Acknowledgements

This work was financially supported by the National Natural Science Foundation of China (Nos. U1360105, U1760201, and 51574192).

References

[1] F. Popa, I. Chicinaş, D. Frunză, I. Nicodim, and D. Banabic, Influence of high deformation on the microstructure of low-carbon steel, *Int. J. Miner. Metall. Mater.*, 21(2014), No. 3, p. 273.

[2] J. Cai, P. Lv, C.L. Zhang, J. Wu, C. Li, and Q.F. Guan, Microstructure and properties of low carbon steel after surface alloying induced by high current pulsed electron beam, *Nucl. Instrum. Methods Phys. Res. Sect. B*, 410(2017), p. 47.

[3] D.M. Sekban, S.M. Akterer, O. Saray, Z.Y. Ma, and G. Purcek, Formability of friction stir processed low carbon steels used in shipbuilding, *J. Mater. Sci. Technol.*, 34(2018), No. 1, p. 237.

[4] E.G. Astafurova, G.G. Zakharova, E.V. Naydenkin, S.V. Dobatkin, and G.I. Raab, Influence of equal-channel angular pressing on the structure and mechanical properties of low-carbon steel 10G2FT, *Phys. Met. Metall.*, 110(2010), No. 3, p. 260.

[5] R.S. Mishra, M.W. Mahoney, S.X. McFadden, N.A. Mara, and A.K. Mukherjee, High strain rate superplasticity in a friction stir processed 7075 Al alloy, *Scripta Mater.*, 42(1999), No. 2, p. 163.

[6] M.S. Khorrami, M. Kazeminezhad, Y. Miyashita, and A.H. Kokabi, Improvement in the mechanical properties of Al/SiC nanocomposites fabricated by severe plastic deformation and friction stir processing, *Int. J. Miner. Metall. Mater.*, 24(2017), No. 3, p. 297.

[7] W.M. Thomas, E.D. Nicholas, J.C. Needham, M.G. Murch, P. Templesmith, C.J. Dawes, *Friction Stir Butt Welding*, Great Britain Patent, Appl. 9125978.8, 1991.

[8] Y.H. Yau, A. Hussain, R.K. Lalwani, H.K. Chan, and N. Hakimi, Temperature distribution study during the friction stir welding process of Al2024-t3 aluminum alloy, *Int. J. Miner. Metall. Mater.*, 20(2013), No. 8, p. 779.

[9] A. Rahbar-kelishami, A. Abdollah-zadeh, M.M. Hadavi, R.A. Seraj, and A.P. Gerlich, Improvement of wear resistance of sprayed layer on 52100 steel by friction stir processing, *Appl. Surf. Sci.*, 316(2014), p. 501.

[10] A. Chabok and K. Dehghani, Formation of nanograin in IF steels by friction stir processing, *Mater. Sci. Eng. A*, 528(2010), No. 1, p. 309.

[11] K. Dehghani and A. Chabok, Dependence of Zener parameter on the nanograins formed during friction stir processing of interstitial free steels, *Mater. Sci. Eng. A*, 528(2011), No. 13-14, p. 4325.

[12] A. Ghasemi-Kahrizsangi and S.F. Kashani-Bozorg, Microstructure and mechanical properties of steel/TiC nano-composite surface layer produced by friction stir processing, *Surf. Coat. Technol.*, 209(2012), p. 15.

[13] R.S. Mishra and Z.Y. Ma, Friction stir welding and processing, *Mater Sci. Eng. R*, 50(2005), No. 1-2, p. 1.

[14] W. Wang, K.S. Wang, Q. Guo, and N. Wu, Effect of friction stir processing on microstructure and mechanical properties of cast AZ31 magnesium alloy, *Rare Met. Mater. Eng.*, 41(2012), No. 9, p. 1522.

[15] A. Chabok and K. Dehghani, Effect of processing parameters on the mechanical properties of interstitial free steel subjected

to friction stir processing, *J. Mater. Eng. Perform.*, 22(2013), No. 5, p. 1324.

[16] M. Hajian, A. Abdollah-zadeh, S.S. Rezaei-Nejad, H. Assadi, S.M.M. Hadavi, K. Chung, and M. Shokouhimehr, Improvement in cavitation erosion resistance of AISI 316L stainless steel by friction stir processing, *Appl. Surf. Sci.*, 308(2014), p. 184.

[17] M. Mehranfar and K. Dehghani, Producing nanostructured super-austenitic steels by friction stir processing, *Mater. Sci. Eng. A*, 528(2011), No. 9, p. 3404.

[18] A. Amirafshar and H. Pouraliakbar, Effect of tool pin design on the microstructural evolutions and tribological characteristics of friction stir processed structural steel, *Measurement*, 68(2015), p. 111.

[19] D.M. Sekban, S.M. Akterer, O. Saray, Z.Y. Ma, and G. Purcek, Formability of friction stir processed low carbon steels used in shipbuilding, *J. Mater. Sci. Technol.*, 34(2018), No. 1, p. 237.

[20] D.M. Sekban, S.M. Aktarer, H. Zhang, P. Xue, Z.Y. Ma, and G. Purcek, Microstructural and mechanical evolution of a low carbon steel by friction stir processing, *Metall. Mater. Trans. A*, 48(2017), No. 8, p. 3869.

[21] Y. Li, F. Wang, and G. Liu, Grain size effect on the electrochemical corrosion behavior of surface nanocrystallized low-carbon steel, *Corrosion*, 60(2004), No. 10, p. 891.

[22] H. Zhang, D. Wang, P. Xue, L.H. Wu, D.R. Ni, and Z.Y. Ma, Microstructural evolution and pitting corrosion behavior of friction stir welded joint of high nitrogen stainless steel, *Mater. Des.*, 110(2016), p. 802.

[23] T. Yingsamphancharoen, N. Srisuwan, and A. Rodchanarowan, The electrochemical investigation of the corrosion rates of welded pipe ASTMA106 grade B, *Metals*, 6(2016), No. 9, p. 207.

[24] P. Xue, W.D. Li, D. Wang, W.G. Wang, B.L. Xiao, and Z.Y. Ma, Enhanced mechanical properties of medium carbon steel casting via friction stir processing and subsequent annealing, *Mater. Sci. Eng. A*, 670(2016), p. 153.

[25] P. Xue, B.L. Xiao, W.G. Wang, Q. Zhang, D. Wang, Q.Z. Wang, and Z.Y. Ma, Achieving ultrafine dual-phase structure with superior mechanical property in friction stir processed plain low carbon steel, *Mater. Sci. Eng. A*, 575(2013), p. 30.

[26] S.C. Li, G.M. Zhu, and Y.L. Kang, Effect of substructure on mechanical properties and fracture behavior of lath martensite in 0.1C 1.1Si 1.7Mn steel, *J. Alloys Compd.*, 675(2016), p. 104.

[27] Z.J. Luo, L.P. Wang, M. Wang, J.C. Shen, and H. Su, Effect of lath martensite/bainite microstructure on strength and toughness of a low carbon martensite steel, *Trans. Mater. Heat Treat.*, 33(2012), No. 2, p. 85.

[28] S.H. Lee, Y. Saito, K.T. Park, and D.H. Shin, Microstructures and mechanical properties of ultra low carbon if steel processed by accumulative roll bonding process, *Mater. Trans.*, 43(2002), No. 9, p. 2320.

[29] R.B. Singh, N.K. Mukhopadhyay, G.V.S. Sastry, and R. Manna, Development of high-strength bulk ultrafine-grained low carbon steel produced by equal-channel angular pressing, *Metall. Mater. Trans. A*, 48(2017), No. 11, p. 5449.

[30] L.Y. Huang, K.S. Wang, W. Wang, K. Zhao, J. Yuan, Q. Wang, K. Qiao, and J. Cai, Corrosion properties of low carbon steel prepared by submerged friction stir processing, *Mater. Corros.*, 69(2018), No. 8, p. 1077.

[31] E. Ura-Bińczyk, A. Dobkowska, M. Płocińska, T. Płociński, B. Adamczyk-Cieślak, B. Mazurkiewicz, W. Solarski, J. Banaś, and J. Mizera, The influence of grain refinement on the corrosion rate of carbon steels in fracturing fluids used in shale gas production, *Mater. Corros.*, 68(2017), No. 11, p. 1190.

[32] Q. Bai, Y. Zuo, X.F. Kong, Y. Gao, S. Dong, and W. Zhang, The influence of the corrosion product layer generated on the high strength low-alloy steels welded by underwater wet welding with stainless steel electrodes in seawater, *J. Ocean Univ. China*, 16(2017), No. 1, p. 49.